

# The Aonia-Solis-Valles dust storm track in the southern hemisphere of Mars

Michael Battalio\*, Huiqun Wang

Harvard-Smithsonian Center for Astrophysics, Smithsonian Astrophysical Observatory, MS 50, 60 Garden Street, Cambridge, MA 02138, United States

## ARTICLE INFO

### Keywords:

Atmospheres, dynamics  
Mars, atmosphere  
Mars, climate

## ABSTRACT

Dust storm activity in the Aonia-Solis-Valles Marineris (ASV) region is analyzed using data collected from 8 Mars years of Mars Daily Global Maps. During  $L_s = 120^\circ$ – $180^\circ$ , dust storms within the ASV region tend to organize into dust storm sequences, making ASV an important storm track in the southern hemisphere outside the conventional dust storm season. In late southern winter, the ASV region is influenced by a combination of strong time-mean winds, synoptic eddies, and tidal winds. The ASV dust storm sequences can increase the background dust opacity and sometimes significantly influence the large-scale atmospheric thermal structure and planetary waves. They can be divided into two groups – one with large size and long duration; the other with small size and mostly short duration. The time series of storm area exhibits a pseudo-periodicity near 20 sols. This periodicity is similar to that found in eddy kinetic energy and traveling waves and to the Baroclinic Annular Mode of the terrestrial atmosphere.

## 1. Introduction

Dust is critical to the Martian atmosphere. It influences atmospheric circulation via radiative heating/cooling. Conversely, its distribution is determined by atmospheric circulation through dust lifting, mixing, transportation, and deposition. This radiative-dynamic feedback is intrinsically linked to the variability of the Martian atmosphere and dust cycle.

Dust storms play an important role in the Martian dust cycle. They are traditionally classified into local, regional and planet-encircling dust storms according to sizes (Martin and Zurek, 1993). While small dust storms occur throughout the year, large dust storms are most active during the northern fall and winter dust storm season (Cantor, 2007). A dust storm that spreads large enough and lasts long enough can significantly affect the visibility, thermal structure and atmospheric circulation (Kass et al., 2016; Toigo et al., 2018). These major dust storms result from dust storm sequences that follow specific trajectories and display coherent development histories (Wang and Richardson, 2015).

Previous studies mostly concentrated on the major dust storms during the dust storm season (northern fall and winter). Those dust storms primarily develop from dust storm sequences originating from Acidalia, Utopia, and Hellas (Wang and Richardson, 2015).

The dust storms in the Aonia-Solis-Valles Marineris region ( $0^\circ$ – $100^\circ$ W,  $0^\circ$ – $46^\circ$ S, called “ASV” for brevity) form dust storm sequences that represent the most important dust activity outside the dust

storm season. Their special seasonality contributes significantly to the annual cycle of atmospheric dust opacity. Despite being less pronounced than the major dust storms during the dust storm season, large ASV sequences can sometimes affect the global atmospheric dynamics and circulation. The year-to-year change of dust activity in the ASV region comprises an integral part of the variability of the Martian atmosphere. Thus, this paper examines the detailed distribution of the dust storms and dust storm sequences in the ASV region.

## 2. Data and methods

Data for the ASV dust storms are collected using Mars Daily Global Maps (MDGMs) from Mars Year (MY) 24–31. These MDGMs include the Mars Global Surveyor (MGS) Mars Orbiter Camera (MOC) set (from MY 24  $L_s = 150^\circ$  to MY 28  $L_s = 121^\circ$ ) and the Mars Reconnaissance Orbiter (MRO) Mars Color Imager (MARCI) set (from MY 28  $L_s = 133^\circ$  to MY 32  $L_s = 110^\circ$ ). Each MDGM is on a  $0.1^\circ$  longitude  $\times$   $0.1^\circ$  latitude grid and is composed of 13 consecutive sets of global image swaths taken during the course of about one day. Each MRO MDGM covers  $90^\circ$ N– $90^\circ$ S. Each MGS MDGM is separated into a north polar ( $45^\circ$ N– $90^\circ$ N), a south polar ( $45^\circ$ S– $90^\circ$ S) and a non-polar ( $60^\circ$ S– $60^\circ$ N) map due to historical reasons (Wang and Ingersoll, 2002). For the MGS years, only the non-polar MDGMs are used in this study; for the MRO years, the whole planet is examined using Version 2 MARCI MDGMs. Version 2 MARCI MDGMs have undergone additional normalization to improve image quality, and occasionally the swaths used for each sol of

\* Corresponding author.

E-mail address: [michael@battalio.com](mailto:michael@battalio.com) (M. Battalio).

<https://doi.org/10.1016/j.icarus.2018.10.026>

Received 15 August 2018; Received in revised form 22 October 2018; Accepted 25 October 2018

Available online 14 November 2018

0019-1035/ © 2018 Elsevier Inc. All rights reserved.

the Version 2 maps are different from version 1. However, the dust storm statistics should be the same for both versions. The data collected are primarily for the  $L_s = 120^\circ$ – $180^\circ$  season.

Dust storms with clear optical contrast have well-defined boundaries and are easily identifiable in MDGMs. Dust storm boundaries are outlined manually in MDGMs (following e.g., Guzewich et al., 2015; Kulowski et al., 2017). A confidence level is assigned to each storm (25, 50, 75, or 100%) to indicate the accuracy of the storm edge. Only storms with a confidence interval of 50% or above are analyzed in this paper. Replication of the analysis with a confidence of 75% or larger does not significantly alter the results. The data are used to calculate dust storm areas and centroids. In addition, the existence of texture (Kulowski et al., 2017) is recorded for each instance. A unique identifier is given to each dust storm so that the storm can be tracked if it lasts for multiple days. In the event of missing data interrupting the tracking of a storm, a new identifier is assigned. A single dust storm can split into separate storms. Multiple dust storms can combine into a single storm.

Following Wang and Richardson (2015), a group of two or more dust storms is identified as belonging to a dust storm *sequence* with the individual storms called *members* of the sequence if the following criteria are satisfied: (1) The collection of dust storm members sustains a duration of three or more sols, i.e., there is no break in dust storm activity throughout the lifetime of the sequence; (2) Dust storm members remain distinct from the background dust opacity that can be either low or high; (3) Dust storm members follow a general trajectory during the development of a sequence. Thus, each sequence must last longer than three sols, but individual members of a sequence can each last as short as one sol or as long as the whole sequence. Each dust storm sequence is attached to a unique sequence ID. This makes it possible to separate organized dust events from isolated dust storms. As a result, the role of dust storm sequences can be assessed in the Martian dust cycle.

This paper mainly focuses on the dust storms in the ASV region during  $L_s = 120^\circ$ – $180^\circ$ . As will be shown in Section 3.1, this is the time period when the ASV dust storms form sequences that significantly influence the annual dust cycle. A few cases extending just beyond  $L_s = 180^\circ$  are included for completeness. Included with the supplementary material is a csv file containing the time, location, and area of all dust storms for  $L_s = 120^\circ$ – $180^\circ$  from MY 24–31.

In a few occasions, auxiliary datasets are used to interpret the data. These datasets include the Mars Analysis Correction Data Assimilation v1.0 (MACDA) reanalysis dataset ( $5^\circ$  longitude  $\times$   $5^\circ$  latitude  $\times$  25 sigma levels, Montabone et al., 2014), the Montabone et al. (2015)  $3^\circ$  longitude  $\times$   $3^\circ$  latitude 9 micron absorption dust optical depth, and the Version 4 MRO Mars Climate Sounder (MCS) temperature profile retrievals (Kleinböhl et al., 2009).

## 3. Results

### 3.1. Temporal context

Fig. 1 shows the global annual cycle of the dust storms identified in MDGMs and the background dust opacity for MY 29. Similar plots for additional Mars years can be found in the supplementary material of this paper. The general distribution is similar across the years, though the detailed distribution exhibits inter-annual variability. The background dust opacity is defined here as the zonal-mean dust optical depth at 610 Pa calculated using the Montabone et al. (2015) dataset. The superimposed symbols indicate the timing and latitudes of the dust storms, with the symbol sizes proportional to the storm areas. The vertical lines associated with the symbols correspond to the latitudinal extents of the storms. In accordance with the result of Guzewich et al. (2017), most dust storms follow the polar cap edges, and fewer dust storms are observed near the summer/winter solstices than during the rest of the year. The latter reflects the solstitial pauses of transient eddies in the lower atmosphere (Lewis et al., 2016).

Fig. 1 suggests that the dust storms that make the most difference to the background dust opacity are the ones that progress from the cap edges toward lower latitudes. These dust storms occur in clusters. They form dust storm sequences that lead to pronounced enhancement of background dust opacity over the annual cycle. The  $L_s = 220^\circ$ – $237^\circ$  major dust storm originates from Acidalia, and the  $L_s = 305^\circ$ – $316^\circ$  major dust storm originates from Utopia. Major dust storms from Acidalia and Arcadia start at  $L_s = 322^\circ$ , shortly before the missing data period at the end of the year. Besides these northern fall and winter events, the most significant episodes originate from the southern hemisphere during mid/late southern winter. Thus, the  $L_s = 120^\circ$ – $180^\circ$  period is the focus of this study.

Southern hemisphere dust storms are also active before the southern winter solstice (Fig. 1). However, the pre-solstice dust storms are generally smaller in size and shorter in duration than the ones during  $L_s = 120^\circ$ – $180^\circ$  and have limited impact on the background dust opacity (Fig. 1). In accordance, Battalio et al. (2018) found that the domain averaged eddy kinetic energy (EKE) for  $57.5^\circ$ – $82.5^\circ$ S is the strongest during  $L_s = 120^\circ$ – $180^\circ$ , the second strongest during  $L_s = 0^\circ$ – $60^\circ$ , and the weakest during  $L_s = 60^\circ$ – $120^\circ$ . The asymmetric seasonality of synoptic transient eddies are also seen in the EMARS reanalysis (Greybush et al., 2019) and free-running GCMs when radiatively active clouds are included (Mulholland et al., 2016; Lee et al., 2018). Battalio et al. (2018) also showed that the synoptic eddies after the southern winter solstitial pause are associated with more vigorous barotropic and baroclinic energy conversion.

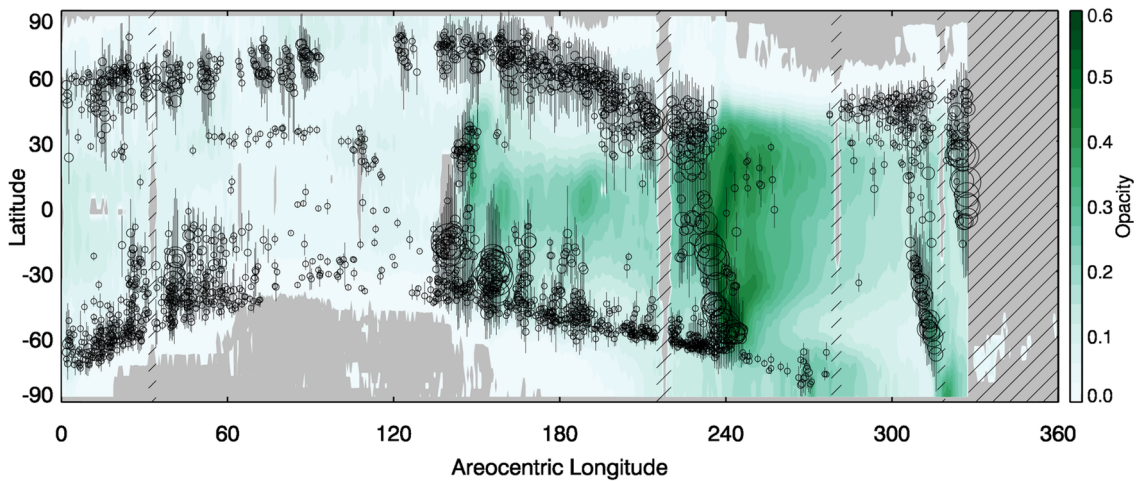
### 3.2. Spatial distribution

Fig. 2 shows the spatial distribution of the dust storms identified in MDGMs during  $L_s = 120^\circ$ – $180^\circ$  for the MOC set (MY 24–27, top) and the MARCI set (MY 28–31, bottom). The circles indicate dust storm centroids, and the symbol sizes are proportional to storm areas. Northern hemisphere storms are clustered along the edge of the polar cap, with the largest concentration in northern Acidalia. Southern hemisphere storms are also observed near the edge of the polar cap with apparent equatorward extension from Hellas, Cimmeria/Sirenum, and Aonia/Argyre. Among the three regions, the region north of Aonia/Argyre extends the closest to the equator and has the densest concentration of dust storms in southern mid/low latitudes. This region is approximately between  $0^\circ$ – $100^\circ$ W and  $0^\circ$ – $46^\circ$ S and is the ASV region introduced in Section 1.

Fig. 3 shows the occurrence frequency map of dust storms for  $L_s = 120^\circ$ – $180^\circ$  derived from MY 24–31. It is based on the same dataset as that used in Fig. 2 but shows the areal extent of the areas affected by dust storms. For each  $0.1^\circ \times 0.1^\circ$  MDGM pixel, the number of sols with dust storm activity is divided by the total number of MDGMs for that point. The discontinuity at  $60^\circ$ N/S is due to the edge of the non-polar MOC MDGMs.

The southern hemisphere has a prominent zonal band of dust activity between  $40^\circ$  and  $60^\circ$ S (Fig. 3). Within this band, there are three local maxima in occurrence frequency, including northwestern Hellas, southern Aonia (west of Argyre), and southern Cimmeria/Sirenum. Equatorward of  $40^\circ$ S, northern Cimmeria/Sirenum, northern Hellas, and the ASV region show frequent dust storm activity. Among these, the ASV region reaches the furthest north and is the main region hosting equator-bound dust storm sequences during  $L_s = 120^\circ$ – $180^\circ$  (Section 3.3). The high elevation of Solis/Aonia implies low atmospheric density and therefore low surface wind stress, if other factors are identical. However, Mulholland et al. (2015) showed that the low surface wind stress in the south might be offset by the increased gustiness in models in the southern hemisphere subtropical latitudes during spring and summer. Although the northern circumpolar area has a higher storm occurrence frequency, the northern hemisphere dust storms do not extend south of  $40^\circ$ N during this season.

The wind vectors in Fig. 3 are the time-mean winds during  $L_s =$



**Fig. 1.**  $L_s$  - latitude distribution of dust storms and background dust for MY 29. Circles indicate dust storm centroids. Circle size is scaled by storm area. Vertical lines associated with circles indicate latitudinal extents of storms. Zonally averaged dust optical depth [from Montabone et al. (2015) and scaled to 610 Pa] is shaded in green. Gray shading indicates missing opacity data. Areas with hatching indicate time periods of missing MDGMs. (For interpretation of the references to color in this figure legend, the reader is referred to the web version of this article.)

120°–180° at roughly  $z \sim 0.6$  km above the surface ( $\sigma = 0.9426$ ). They are calculated using MACDA from both MY 25 and 26. This vertical level is chosen because it corresponds to the height of the maximum in the meridional-averaged (2.5°–47.5°S) winds below 5 km. There is a clear correspondence between the dust storm frequency and the wind pattern in the southern hemisphere. In particular, strong northward winds exist to the west of Hellas, in the eastern part of the ASV region, and (to a lesser degree) in northern Cimberia/Sirenum. Among these areas, the ASV branch extends the closest to the equator. These winds are co-located with the northward extension of increased dust storm frequency.

In addition, the ASV region is also affected by strong synoptic and tidal winds during  $L_s = 120^\circ$ –180°. Fig. 4 shows the 90th percentiles of 1.5–8 sol synoptic and  $\leq 1$  sol tidal EKE at  $z \sim 0.6$  km. Results are derived from MACDA MY 24  $L_s = 145^\circ$ –180°. [Note that the shortened window due to the start time of the MACDA dataset in MY 24 may influence the average amplitude of the waves. However, MY 24 was chosen because MY 25 began to show influences from the 2001 global dust storm, and MY 26 had issues from a bias in TES retrievals (Pankine, 2015; 2016).] The range of wave periods for synoptic eddies corresponds to the observed durations of dust storms and dust storm sequences (Section 3.4). This range also reflects the periods of synoptic eddies commonly observed in other datasets (Barnes, 1981; Banfield et al., 2004). The tidal winds include diurnal, semi-diurnal, and other harmonic contributions.

For the ASV region, while the area to the north of Argyre is controlled by strong time-mean winds (Fig. 3), the area in southern Aonia (west of Argyre) is controlled by strong synoptic winds (Fig. 4a). Southern Aonia is associated with the maximum EKE and baroclinic growth rate in the southern hemisphere after the southern winter solstice (Battalio et al., 2018). The barotropic conversion of energy is also maximized to the west of Argyre (Battalio et al., 2018). The western part of the ASV region is influenced by strong tidal winds along the Tharsis slopes (Fig. 4b). Thus, the combination of strong time-mean winds, synoptic winds, and tidal winds make the ASV region a preferred candidate for dust storms in mid/late southern winter. The localization of eddies in the zonal direction between 90° and 300° E in the southern hemisphere was noted by Battalio et al. (2018).

### 3.3. Sequence versus non-sequence storms

A key differentiator between the ASV and other regions in terms of dust storm activity during  $L_s = 120^\circ$ –180° is that the dust storms in the

ASV region tend to organize into sequences, while those in other regions are dominated by unrelated events. This is illustrated in Fig. 5, where the data in Fig. 2 are separated into sequence and non-sequence storms. Most of the dust storms around Hellas – as well as much of the dust storms in the zonal band around the cap edge – do not belong to a sequence. In comparison, a substantial percentage ( $\sim 33\%$ ) of the dust storms in the ASV region belongs to a sequence. This makes the ASV region a distinct storm track from Hellas and other regions in the southern hemisphere in mid/late southern winter. Of the 458 dust storms in the ASV region, 151 storms comprise the individual members of 28 dust storm sequences. The remaining 307 storms are not a part of a sequence. All 458 storms have an average size of  $\sim 530,000$  km<sup>2</sup> and duration of  $\sim 1.6$  sols. For the 34% of storms that last longer than one

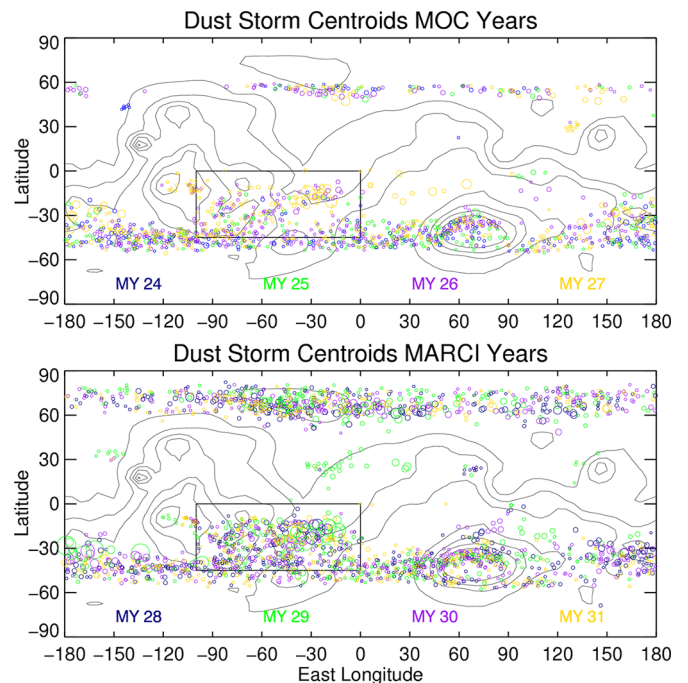


**Fig. 2.** Longitude-latitude distribution of dust storm centroids. Results are for  $L_s = 120^\circ$ –180° of MY 24–27 (top) and MY 28–31 (bottom). Circles are scaled by storm areas. Colors indicate Mars years. Contours indicate topography. The ASV area is outlined with a black box.

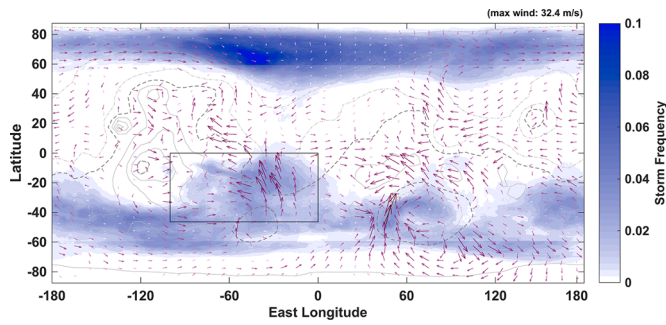


Fig. 3. Dust storm occurrence frequency map for  $L_s = 120^\circ\text{--}180^\circ$  of MY 24–31. Topography is indicated by contours. The ASV region is enclosed in a black box. Time mean winds at  $z \sim 0.6$  km (corresponding to  $\sigma = 0.9426$  in MACDA) for  $L_s = 120^\circ\text{--}180^\circ$  of MY 25–26 are overlaid as vectors.

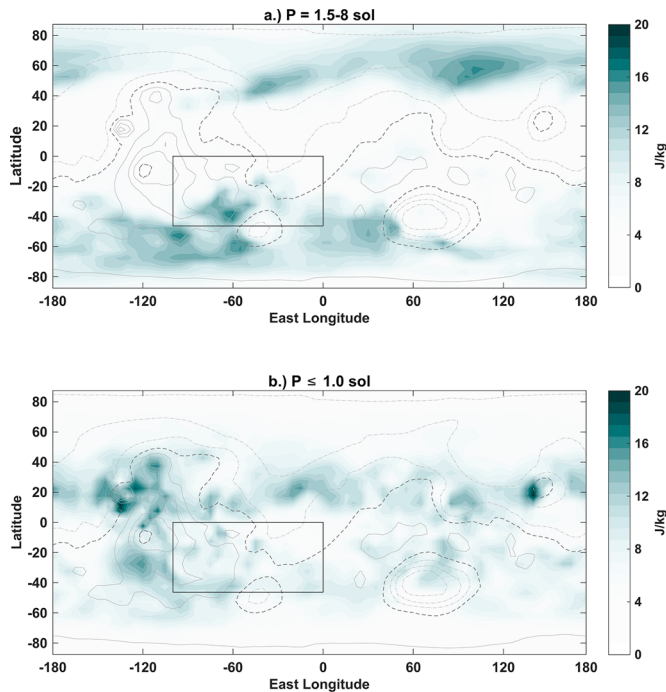


Fig. 4. 90th percentile of eddy kinetic energy for (a) 1.5–8 sol eddies and (b)  $\leq 1$  sol eddies at  $z \sim 0.6$  km (corresponding to  $\sigma = 0.9426$  in MACDA) for  $L_s = 145^\circ\text{--}180^\circ$  of MY 24. The ASV region is indicated by a black box.

sol, the average size and duration are  $\sim 1,190,000$  km<sup>2</sup> and  $\sim 2.9$  sols, respectively. Fig. 6 shows the size distributions of sequence and non-sequence dust storms in the ASV region. While both exhibit an exponential decay with increasing size, the decay rate is much smaller for members of dust storm sequences as opposed to non-sequence dust storms. As a result, the cumulative probability of sequence members climbs slower than that of the non-sequence storms. The mean size of sequence members is  $\sim 1,040,000$  km<sup>2</sup>, which is about 3.7 times that of non-sequence storms ( $\sim 281,000$  km<sup>2</sup>). The median size of sequence members is  $\sim 590,000$  km<sup>2</sup>, which is about 5.1 times that of non-sequence storms ( $\sim 115,000$  km<sup>2</sup>). The average duration of sequence members is  $\sim 2.3$  sols, but for non-sequence storms, the average duration is only  $\sim 1.3$  sols. Therefore, despite being more numerous, non-sequence dust storms are generally smaller in size and shorter in duration than storms that are members of a sequence.

### 3.4. Characteristics of ASV dust storm sequences

The study area for ASV sequences corresponds to the farthest northward extension of dust storm activity away from the south polar

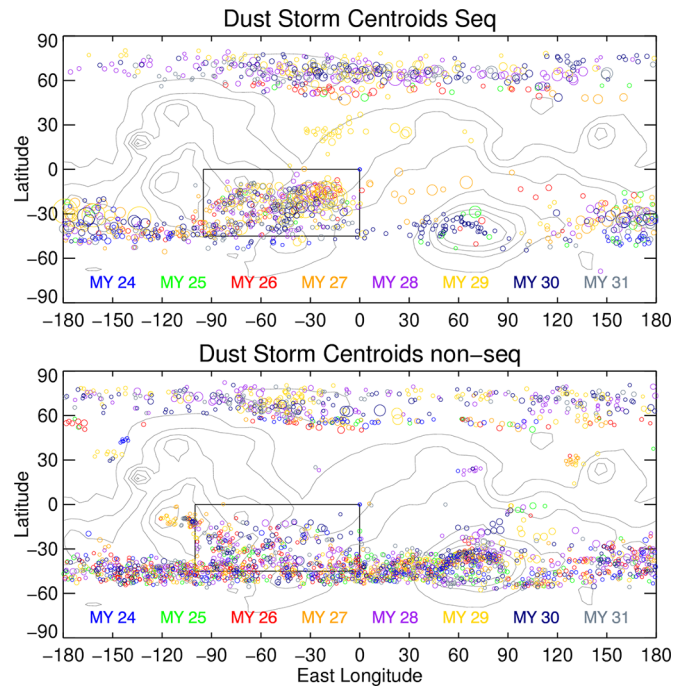


Fig. 5. Same as Fig. 2, but with data separated into sequence and non-sequence dust storms.

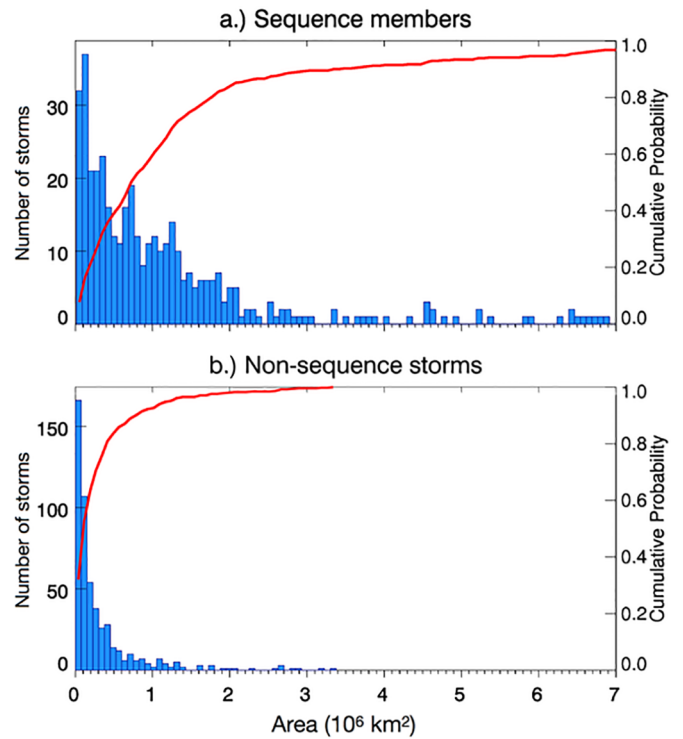


Fig. 6. Histograms for areas of (a) sequence and (b) non-sequence dust storms.

cap during  $L_s = 120^\circ\text{--}180^\circ$  (Figs. 3 and 5). The northern boundary is at the equator. To quantitatively define the southern edge, we examine the latitudes of dust storm centroids. After selecting the dust storms not directly influenced by ASV and Hellas, we find that they approximately follow a normal distribution centered at  $53^\circ\text{S}$  with a standard deviation of  $\sigma = 7^\circ$  of latitude. Therefore, we define the cap edge band center at  $53^\circ\text{S}$  and the southern boundary of ASV at  $46^\circ\text{S}$  ( $1\sigma$  away from the center). The east ( $0^\circ\text{W}$ ) and west edges ( $100^\circ\text{W}$ ) are defined to include

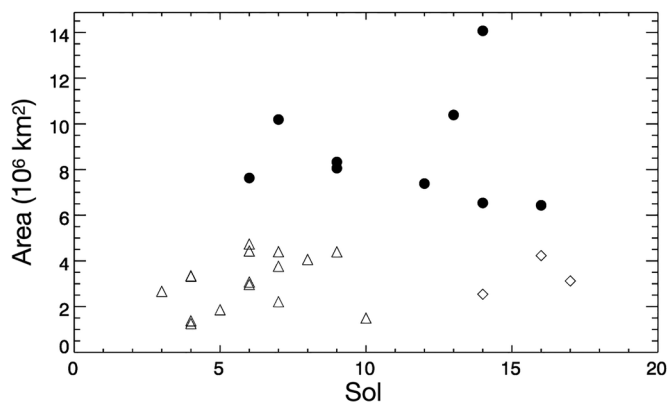


Fig. 7. Scatterplot of dust sequence duration versus maximum area. Group 1 sequences are indicated by filled circles. Group 2 sequences are indicated by open triangles (short duration subgroup) or open diamonds (long duration subgroup).

the area with high dust storm frequency in the ASV region (Fig. 3).

There are a total of 28 dust storm sequences affecting the ASV region. Of those, 20 are generated within ASV; the others are generated elsewhere and advected into ASV. The duration of the sequences varies from 3 to 17 sols and the peak area from 800,000 to 14,000,000 km<sup>2</sup> (Fig. 7). The scatterplot of sequence duration versus peak area indicates two groups (Fig. 7). Group 1 sequences are large (> 6,000,000 km<sup>2</sup>) in areal coverage and long in duration ( $D = 6\text{--}16$  sols, with an average of 12 sols). Group 2 sequences are small (< 6,000,000 km<sup>2</sup>) in areal coverage and have variable durations with an average of  $D = 7$  sols. Most Group 2 sequences are shorter than 7 sols; only 1/6 of them are longer than 10 sols. The threshold area of 6,000,000 km<sup>2</sup> corresponds to a length scale of  $\sim 2,450$  km, which is close to the classical criterion (long-axis > 2000 km) used for the definition of regional dust storm (Martin and Zurek, 1993). It is admittedly somewhat arbitrary, which can influence the classification of sequences close to the threshold. Nevertheless, the tendency of Group 1 sequences being larger and longer than Group 2 sequence is robust.

Fig. 8 shows the day-to-day development of Group 1 (Panel a) and Group 2 (Panel c) sequences. The composite for each group (Fig. 8b & d) is made by averaging the areas for each day of the corresponding sequences. The composite Group 1 sequence has a moderate initial growth rate of  $\sim 1,300,000$  km<sup>2</sup>/sol that levels off as the growth of some sequences is compensated by the decay of others. The maximum sustained (> 5 sols) growth rate ( $\sim 1,800,000$  km<sup>2</sup>/sol) is exhibited by Sequence B2-2, which will be discussed in Section 3.7. The composite Group 2 sequence grows to a maximum of  $\sim 1,900,000$  km<sup>2</sup> in 3 sols, then decreases at  $\sim 310,000$  km<sup>2</sup>/sol afterwards. The symbols in Fig. 8 indicate the instances when > 50% of the dusty area is textured. All sequences begin with a majority of textured activity and progress into a majority of untextured activity. This tendency was also found by Guzewich et al. (2017) and Kulowski et al. (2017). Our results show that in sequences longer than 5 sols, additional textured dust storms occur when secondary dust lifting centers are activated.

The predominant motion of the sequences within ASV is from southeast to northwest, similar to the trajectory in Wang and Richardson (2015). Storms usually originate along the boundary between Solis and Aonia and typically do not travel beyond Margaritifer Terra. Some storms travel from the northwest to the east or southeast after being initiated near Syria Planum, possibly due to the strong tidal winds in the region (Fig. 4b). Occasionally, a dust storm triggered along the cap edge or the rim of Argyre travels north or northwest into the ASV region. Although trajectories from Acidalia, Utopia and Hellas are common during northern fall and winter (Wang and Richardson, 2015), they are not observed during  $L_s = 120^\circ\text{--}180^\circ$ .

### 3.5. Inter-annual variability

Fig. 9 shows the storm area time series of all the dust storms in the southern hemisphere (red) and the dust storms influencing the ASV region (blue). The latter is the sum of two components (1) all non-sequence storms within the ASV region and (2) the total area of all ASV sequence members, regardless of whether or not the dust storm member is partially or completely within ASV. The horizontal bars indicate the time periods when dust storm sequences are active within ASV. During  $L_s = 120^\circ\text{--}200^\circ$ , periods of low dust storm activity are punctuated by episodic large events (Fig. 9). The ASV dust storms account for most of the storm area in the southern hemisphere, underlining the importance of ASV during this time period. The large increase near  $L_s \sim 185^\circ$  in MY 25 is due to a global dust storm originating around Hellas (Strausberg et al., 2005; Cantor, 2007). Fig. 9 also shows that most of the peaks in storm area are associated with dust storm sequences generated within ASV.

There is a wide range of variability across the years. Each year has at least one ASV sequence (e.g., MY 24), but some years have many (e.g., MY 29 has 5). MY 31 appears less active than the previous four years, but it is affected by a prolonged period of missing data. MY 24–27 is covered by MGS MOC with an imaging local time at 2 PM, and MY 28–31 is covered by MRO MARCI with an imaging time at 3 PM. Thus, the increase of dust storm activity from MY 26 to MY 27 is not related to the changing of local time or spacecraft and might represent a climate shift or multi-annual variability.

There are several instances when one sequence immediately follows another (e.g., B2-1 and B2-2, s2-1 and s2-2, G3-1 and G3-2, and D2-1 and D2-2, Fig. 9). In each case, the second sequence is larger than the first one, and the first one is a Group 2 sequence. Two of these precursor sequences have the longest duration in Group 2. The close succession of sequences indicates that a long-duration sequence with limited size may potentially trigger a larger sequence. In other words, a small sequence at the right location that lasts long enough might provide a precondition for an easier growth of thermal-dynamical feedback, allowing a subsequent larger dust storm to develop.

### 3.6. Quasi-periodicity

There appears to be an interesting periodicity in Fig. 9. We perform an FFT on the southern hemisphere time series (red curves in Fig. 9) to transform them into the power spectra in Fig. 10. All years with large sequences (MY 27–31) show a peak between 15 and 20 sols, with an average of 18.5 sols. This signal is particularly strong in MYs 27, 28, 29, and 31. Additionally, some years have a second peak at  $\sim 30$  sols, approximately double the primary period of 15 sols. One interpretation for the 30-sol peak is that  $\sim 15$  sols after a sequence, an attempt for a new sequence fails, but after another  $\sim 15$  sols, a new sequence develops as expected (e.g.,  $L_s \sim 160^\circ$  in MY 28 or  $L_s \sim 148^\circ$  in MY 29). In Earth's southern hemisphere, 20–30 day oscillations are found in the EKE, eddy heat flux, clouds and precipitation (Thompson and Barnes, 2014; Li and Thompson, 2016). These periodicities are attributed to the Baroclinic Annular Mode (BAM) that is related to a negative feedback – growth of baroclinic eddies leads to enhanced poleward heat flux, which in turn reduces the latitudinal temperature gradient and therefore baroclinicity. The temperature gradient must redevelop before the baroclinicity is sufficient to allow the growth of new eddies (Thompson and Barnes, 2014). The similarity in wave periods between our results and the terrestrial BAM inspires us to perform an analysis on EKE using MACDA following the method of Thompson and Woodworth (2014).

First, as in Battalio et al. (2016), we filter out eddies whose wave periods are  $\leq 1$  sol. Then, we calculate the zonal-mean winds  $[u]$  and  $[v]$ . The zonal mean winds are subtracted from the total winds to get the eddies  $u^*$  and  $v^*$  at each grid point. Next, the zonal-mean EKE is calculated as  $[(u^*)^2 + (v^*)^2]/2$  for each latitude and vertical level. The 2-

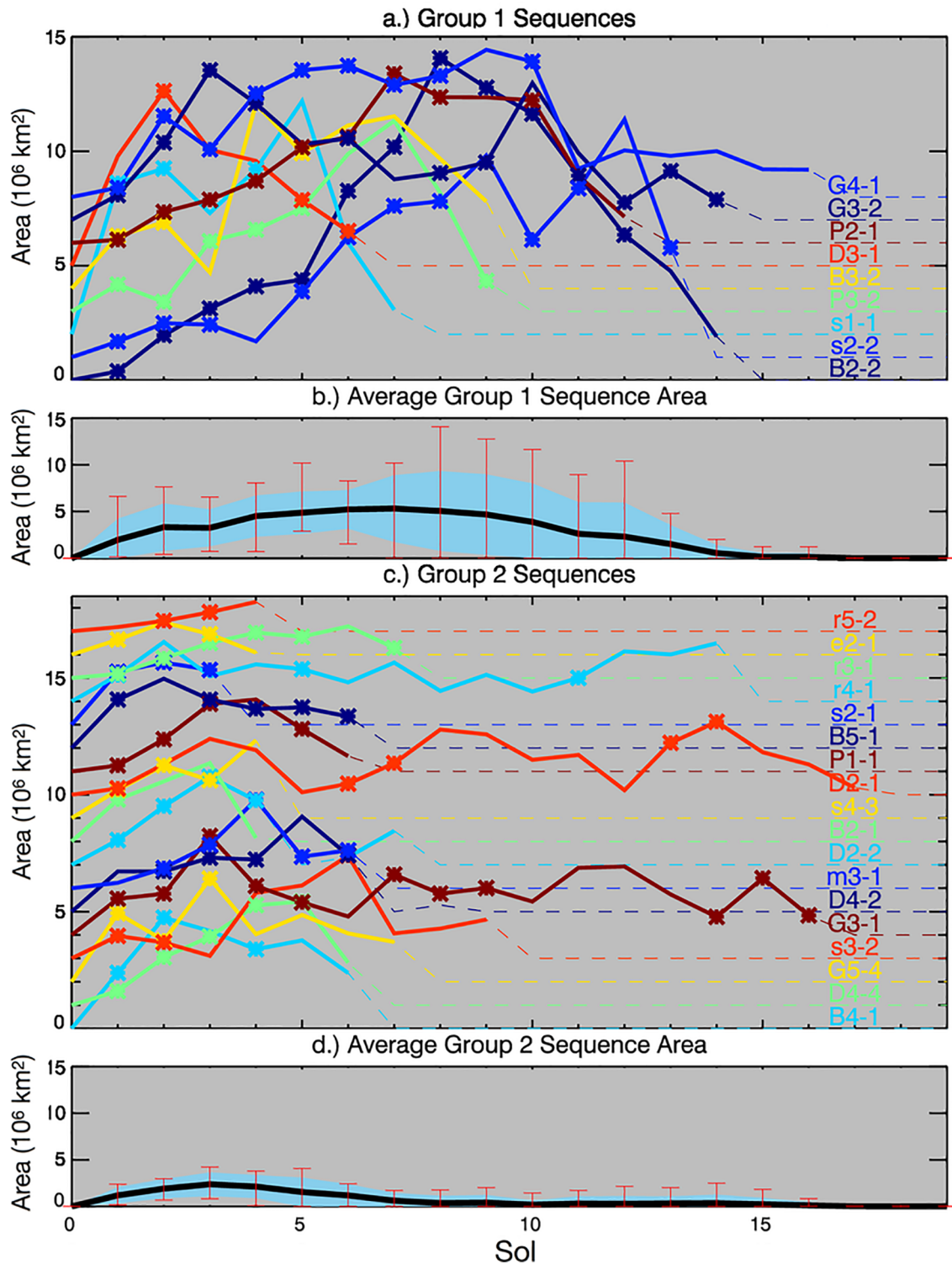


**Fig. 8.** Sol-to-sol development of the areas of dust storm sequences that are generated within ASV. Each sequence is offset by  $10^6 \text{ km}^2$ . The sequence label is listed on right, which is connected by a thin dashed line to each sequence indicated by solid lines. The sequences are ordered by decreasing maximum area from bottom to top. a.) Group 1 sequences of large areal coverage and long duration c.) Group 2 sequences of small areal coverage and variable duration. b.) and d.) Average area for each group. The  $1\sigma$  region is highlighted in blue, the 10th and 90th percentiles in red. (For interpretation of the references to color in this figure legend, the reader is referred to the web version of this article.)

hourly time series is averaged by sol. A 30-sol running mean is removed to obtain the anomalies. Finally, the anomalies are weighted by the square root of the cosine of the latitude and by mass.

The patterns of variability for the  $17.5^\circ\text{--}82.5^\circ\text{S}$  and  $z \sim 0.005\text{--}38 \text{ km}$  (corresponding to  $\sigma = 0.995\text{--}0.022$ ) region are found from an

empirical orthogonal functions (EOF) analysis on the time series of anomalies described above. The leading EOF (Fig. 11b) accounts for  $\sim 42\%$  of the variability. It peaks around  $40^\circ\text{--}60^\circ\text{S}$  at  $z \sim 15 \text{ km}$ , below the jet core. The corresponding Principal Component (PC) clearly shows a quasi-periodicity as it oscillates between positive and negative

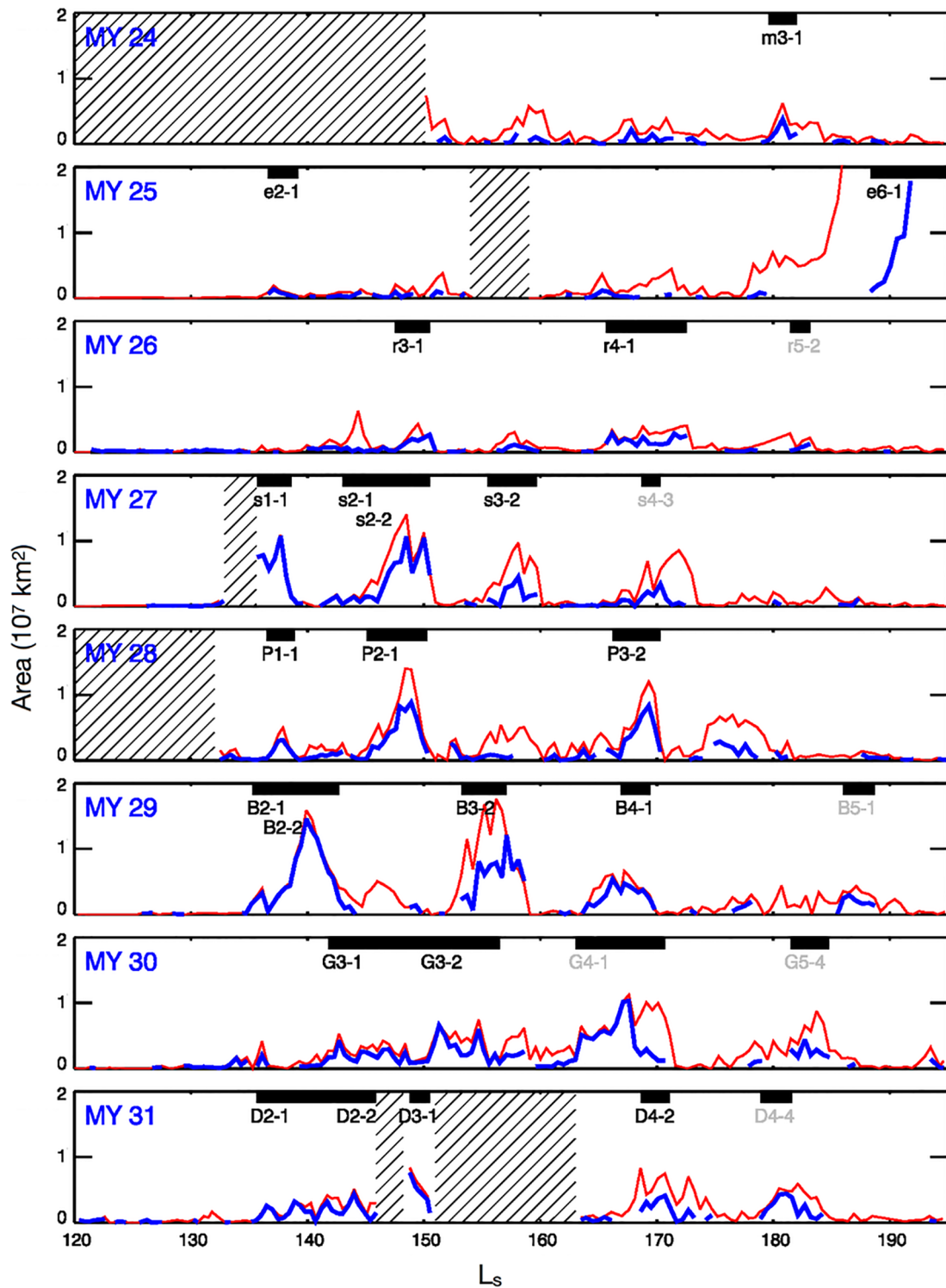


Fig. 9. Areas of dust storms in the southern hemisphere (red) and in/around ASV (blue) as a function of  $L_s$  for MY 24–31. ASV sequences are labeled below thick horizontal bars at the top of each panel. Sequences originating within ASV are in black, while those starting elsewhere are in gray. Time periods without MDGMs are indicated with hatching. (For interpretation of the references to color in this figure legend, the reader is referred to the web version of this article.)

phases (Fig. 11a). The sign of the PC is defined such that positive polarity aligns with higher EKE. Spectral analysis of the PC shows that the most prominent periodicity is  $\sim 20$  sols, similar to that shown by the ASV dust storm area. A second maximum between 3 and 6 sols corresponds to the common periods of transient waves in the lower atmosphere during this season. There also appears to be a correspondence between the positive polarity of the PC and southern hemisphere dust activity (Figs. 9 and 11a). For example, both show peaks just after  $L_s =$

140° (Sequence r3-1) and around  $L_s = 150^\circ$  (Sequence r4-1). An abrupt shift to negative polarity after  $L_s = 180^\circ$  coincides with the end of Sequence r5-2. The positive peaks in MY 24 and 25 also qualitatively match dust activity (not shown). There are instances of large positive PC with no associated dust storms, and vice versa. But, the next EOF (explaining  $\sim 12\%$  of the variability) helps account for this discrepancy (not shown).

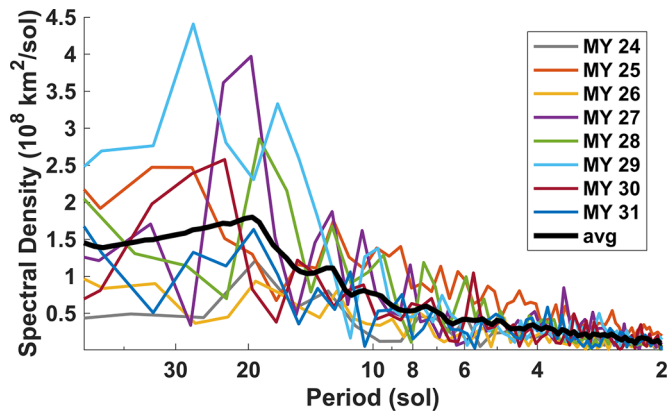


Fig. 10. Spectra derived from the time series of southern hemisphere storm areas. Colors indicate different Mars years. The averaged spectrum is depicted with a thick black line.

### 3.7. The largest ASV sequence

The largest Group 1 sequence during the study period (B2-2) was observed in MY 29 from  $L_s = 137^\circ$  to  $L_s = 143^\circ$  (14 sols). It immediately followed a Group 2 sequence B2-1 ( $L_s = 135^\circ$ – $137^\circ$ , Fig. 9) that resulted from the organization of daily textured dust storms near the polar cap. Sequence B2-2 led to an apparent increase in background dust opacity during  $L_s = 150^\circ$ – $160^\circ$  (Fig. 1). Fig. 12 shows the

development history of Sequence B2-2. The dust storm members of B2-2 are highlighted in green; other dust storms are highlighted in black. Small areas of missing data are interpreted with an educated guess. Large areas of missing data are left out. Each panel is a Version 2 MARCI MDGM.

B2-2 began with a dust storm member ( $\sim 400,000 \text{ km}^2$ ) north of the cap edge along the southern edge of Solis. On the following sol, it moved to the northwest and expanded towards Valles Marineris and occupied  $\sim 2,000,000 \text{ km}^2$ . Texture was noticeable within the dust storm to the north of Argyre. On Sol 3, the textured dust storm moved further north, while a new dust storm member initiated near Solis. By Sol 4, three additional textured dust storms emerged along the Solis rim. The western-most one was the precursor of the largest member of Sequence B2-2. On Sol 5, the precursor grew into a larger ( $\sim 1,600,000 \text{ km}^2$ ), textured, high-opacity dust storm in/around Solis; other dust storm members moved towards Arabia and Noachis Terra. On Sol 6, multiple dust members merged into a large dust storm ( $\sim 6,400,000 \text{ km}^2$ ). On Sols 7, 8, and 9, the large dust storm continued to exhibit texture in Solis. The dusty area reached its maximum of  $\sim 14,000,000 \text{ km}^2$  on Sol 8. On Sol 10, dust became trapped within Valles Marineris and texture disappeared from the main dust storm member. Dust remained thick near the eastern edge of the storm on Sol 11. Thereafter, dust gradually blended into the background as the sequence dissipated.

During the lifetime of B2-2, especially after the formation of the largest dust storm member, several non B2-2 dust storms were observed in the vicinity (Fig. 12). These satellite dust storms were located either to the east of B2-2 within the cap edge zonal band (Sol 5–9, 11–14) or to

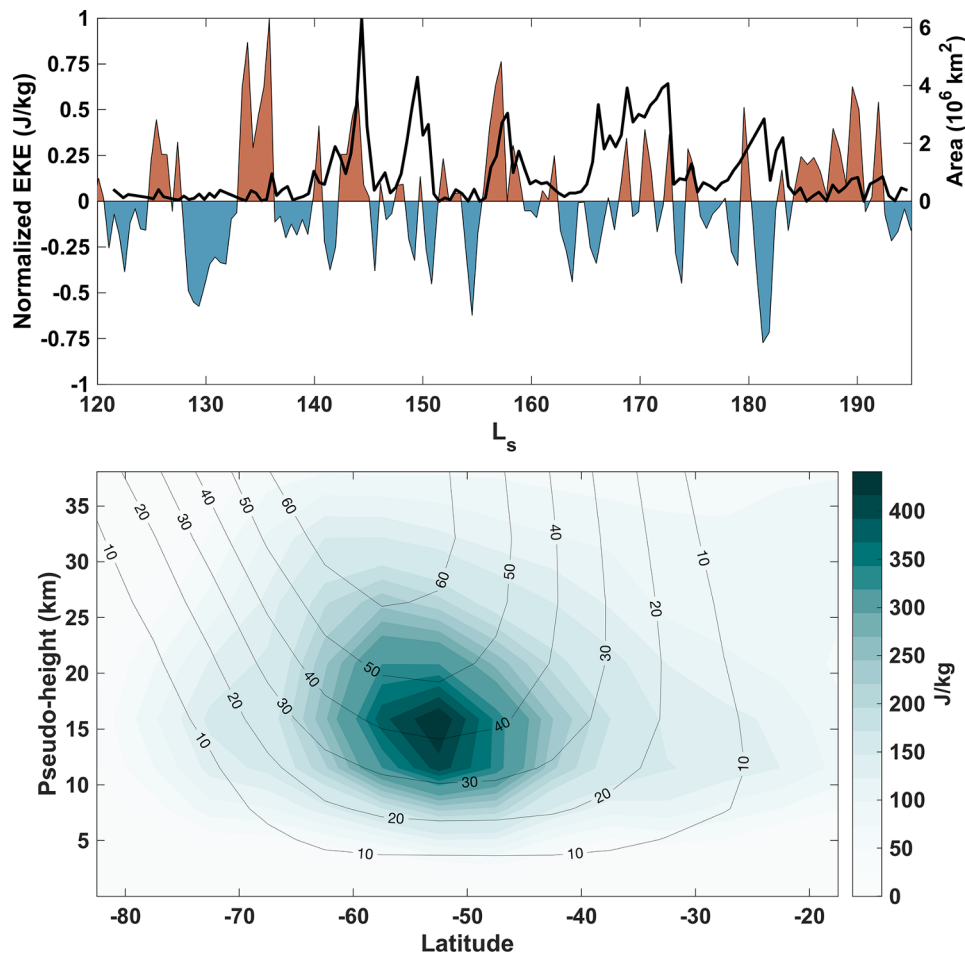
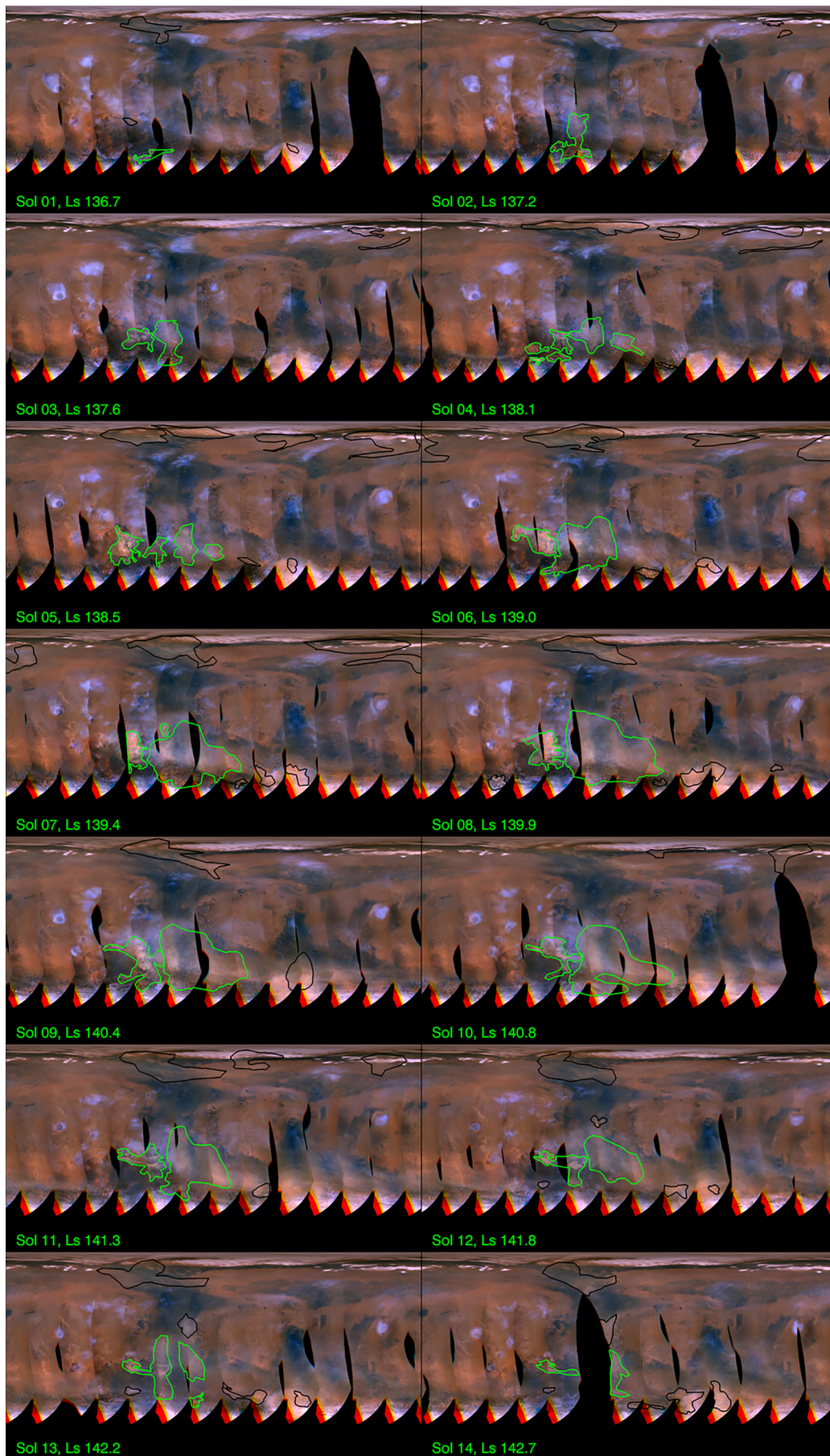


Fig. 11. (Top) The first principal component of the zonal-mean EKE for the region between  $17.5^\circ$  and  $82.7^\circ\text{S}$  for MY 26. The magnitude is normalized by the maximum value. The total area of southern hemisphere dust storms for MY 26 is over plotted in black. (Bottom) The first empirical orthogonal function of the zonal-mean EKE for  $L_s = 120^\circ$ – $195^\circ$  MY 26. The zonal-mean wind is superimposed as contours.



(caption on next page)

**Fig. 12.** Development of Sequence B2-2 during  $L_s = 136.7^\circ\text{--}142.7^\circ$  in MY 29. Storm members of B2-2 are outlined in green, other dust storms are in black. Sol number and  $L_s$  are labeled in the bottom left of each panel. (For interpretation of the references to color in this figure legend, the reader is referred to the web version of this article.)

the north of B2-2 in Chryse (Sol 12–14). While cap edge dust storms are common during  $L_s = 120^\circ\text{--}180^\circ$ , Chryse dust storms are rare during this season. In fact, this is the only case when a Chryse sequence was observed within our study period. The Chryse sequence lasted an additional 11 sols after Sol 14 of Fig. 12. The atypical Chryse sequence may have been triggered by B2-2, which had been developing for 12 sols and was quite large at the time (6,500,000 km<sup>2</sup>). If this is the case, then it supports the modeling result that a long and large dust storm can potentially trigger dust lifting in its vicinity (Toigo et al., 2018).

Sequence B2-2 was associated with a clear signature in mid-level air temperature on a global scale. This is illustrated in Fig. 13 using the zonal mean MCS temperatures for MY 29. The MCS data for each pressure level are first calculated for each day on a  $4^\circ$  latitude  $\times$   $5^\circ$  longitude grid with a bin size of  $4^\circ$  latitude  $\times$   $30^\circ$  longitude  $\times$  8 day. The bins with less than 16 data points are assigned to a missing value. Then, the gridded data on each pressure level are zonally averaged for that day. The latitudes with less than 75% of valid data are assigned to a missing value. The results for  $p \sim 9.8$  Pa ( $z \sim 45$  km) between  $L_s =$

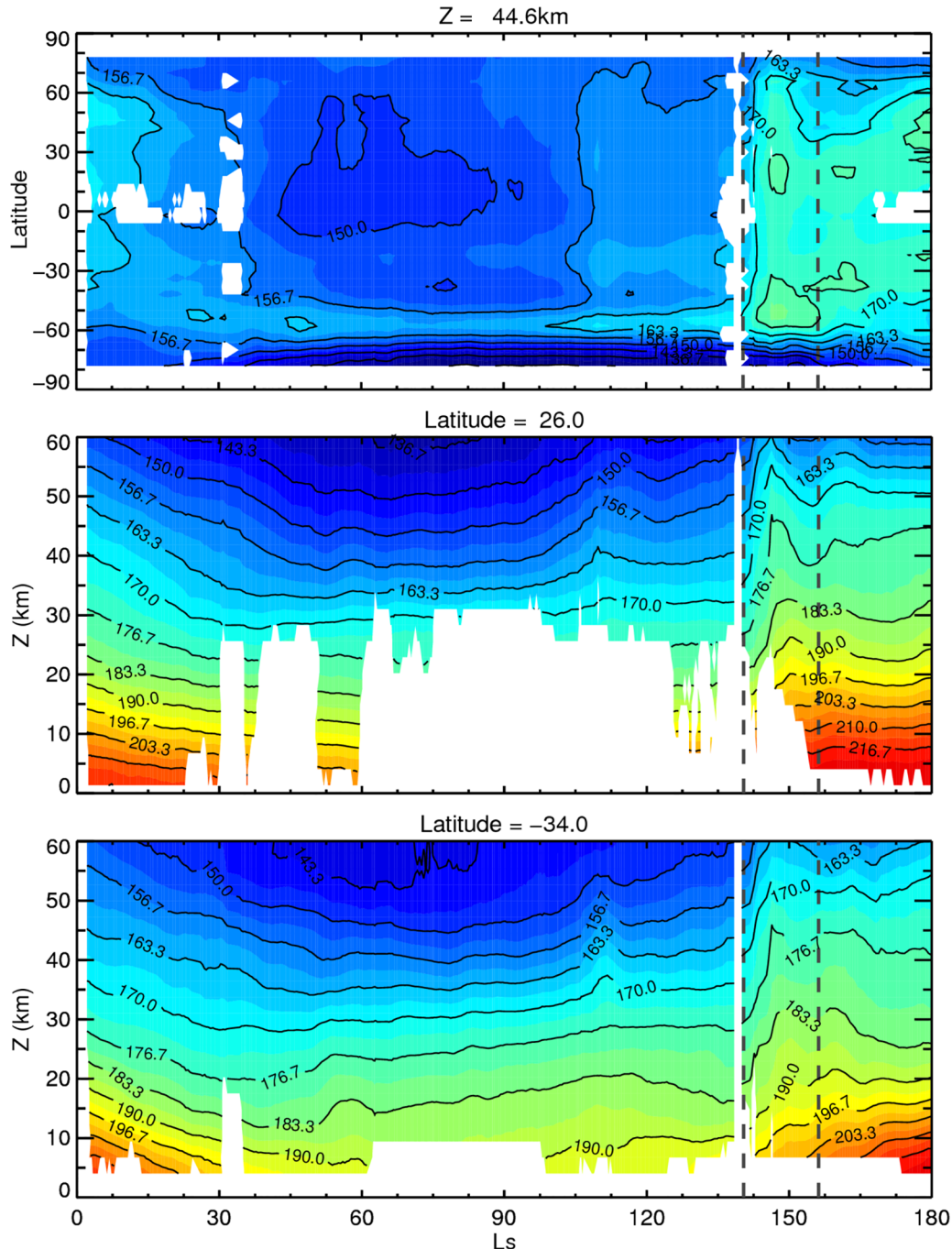


**Fig. 13.** Zonal mean MCS temperature for MY 29. (a)  $L_s$  versus latitude distribution at  $z \sim 45$  km (b, c)  $L_s$  versus height cross sections at  $26^\circ\text{N}$  and  $34^\circ\text{S}$ . The two vertical dashed lines indicate the  $L_s$  of the peak area for sequences B2-2 and B3-2.

$0^\circ$  and  $L_s = 180^\circ$  are combined and plotted in the top panel of Fig. 13.

Significant warming was observed during  $L_s = 140^\circ$ – $150^\circ$  in both the southern and northern hemispheres up to the high latitudes (Fig. 13). The warming immediately followed the peak area of B2-2 (dashed line at  $L_s = 140.4^\circ$ ), indicating the global influence the sequence had on atmospheric thermal structure and circulation. The next sequence in MY 29 – Sequence B3-2 – was observed during  $L_s = 154^\circ$ – $160^\circ$  (peaking at  $L_s = 156.2^\circ$  and indicated in Fig. 13), with a peak size ( $13,000,000 \text{ km}^2$ ),  $\sim 7\%$  smaller than that of B2-2. B3-2 was also associated with a temperature increase, though the anomaly spanned a smaller latitude range.

The bottom two panels of Fig. 13 show the  $L_s$  versus height cross sections of the zonal mean atmospheric temperatures at  $26^\circ\text{N}$  and  $34^\circ\text{S}$ , respectively. The high temperature anomaly associated with Sequence B2-2 clearly extended throughout the atmospheric column below  $z \sim 60 \text{ km}$ . The signatures of Sequence B3-2 were also noticeable above  $z \sim 20 \text{ km}$ . Although southern hemisphere sequences seldom attain the size of B2-2, Fig. 13 demonstrates that this can happen in Mars years with large ASV dust storm sequences.

Sequence B2-2 was also associated with significant changes in traveling waves. Fig. 14 shows the 15–30 day traveling waves derived from the MCS temperature data at  $p \sim 9.8 \text{ Pa}$  for MY 29. For this figure, the MCS data are first processed following the procedure used for Fig. 13 but using a time window of 15 or 30 days; then the difference between the 15-day and 30-day results are plotted as a function of longitude and  $L_s$  for  $50^\circ\text{S}$  and  $50^\circ\text{N}$ . The bins without enough data points are left blank (14 for 15-sol average, 28 for 30-sol average). Despite the data gap between  $L_s \sim 135^\circ$  and  $L_s \sim 145^\circ$ , pronounced enhancements of 15–30 sol waves were observed following Sequence B2-2 and B3-2 in late southern winter

( $L_s = 150^\circ$ – $180^\circ$ , Fig. 9). The waves were dominated by an eastward traveling zonal wavenumber  $m = 1$  mode. The wave periods agree with the periodicity identified in Section 3.6. The  $m = 1$  wave probably had global coherence, as it was observed in both the southern and northern hemispheres. It exemplifies significant perturbations to the global circulation by Sequences B2-2 and B3-2.

Note that although  $m = 1$  waves have large eddy temperature in the middle atmosphere, they usually do not dominate near the surface (Banfield et al., 2004; Lewis et al., 2016). For MY 29, the 2–5 sol eastward traveling  $m = 3$  waves dominate the eddy temperature near the surface during  $L_s = 150^\circ$ – $180^\circ$  (not shown). Traveling waves with  $m = 3$  are common near the south polar cap edge in late winter, as shown by reanalyses (Lewis et al., 2016; Greybush et al., 2019), GCM simulations (Lee et al., 2018) and other observations (Hinson and Wilson, 2002).

#### 4. Summary and discussion

Eight Mars years (MY) of Mars Daily Global Maps (MDGMs) are used to study dust storm activity in the Aonia-Solis-Valles Marineris (ASV) region ( $0^\circ$ – $100^\circ\text{W}$ ,  $0^\circ$ – $46^\circ\text{S}$ ). This region hosts the most important dust storm activity in the southern hemisphere outside the conventional dust storm season, making it the most intense storm track during southern fall and winter.

The dust storms within ASV clearly exhibit a solstitial pause where there is reduced activity near the southern winter solstice ( $L_s = 90^\circ$ ). The ASV track is most active during  $L_s = 120^\circ$ – $180^\circ$  when dust storms tend to organize into dust storm sequences. Dust storms involved in sequences tend to be larger than those that are not. As a consequence, the post-solstice dust storms and sequences are larger and last longer than their pre-solstice counterparts.

The ASV storm track contributes to the annual cycle of background dust and the inter-annual variability of the Martian dust cycle. During mid/late southern winter, the ASV region is influenced by strong synoptic eddies in the south, strong time-mean winds in the east, and strong tidal winds in the west.

The sequences examined in this study can be divided into two groups – Group 1 is large in areal extent ( $> 6,000,000 \text{ km}^2$ ) and long in duration ( $\geq 6$  sols); Group 2 is small in extent and mostly shorter than 7 sols. Sequences generally develop from the southeast toward the northwest, with active dust lifting in Solis and near the south polar cap. This separation of dust sequences into two groups is a demonstration of the effect proposed by Toigo et al. (2018). This suggests that dust storms that achieve a threshold size and duration can regenerate and sustain themselves.

The ASV region has large inter-annual variability in the size and number of sequences. Some years have only one ASV sequence, while others have up to 5. MYs 27–31 appear to be more active than previous Mars years.

There appears to be a distinct 15–20 sol cycle in the time series of dust storm area. In the current absence of numerical weather prediction for Mars, the quasi-periodicity might provide some empirical guidance on dust storm activity. The  $\sim 20$ -sol periodicity is also found in the first principal component of the zonal-mean eddy kinetic energy of the southern hemisphere of Mars. For the southern hemisphere of the Earth, the 25-day oscillation in eddy kinetic energy and other variables is explained as the Baroclinic Annular Mode (BAM) (Thompson and Barnes, 2014).

The largest ASV sequence ( $L_s = 137^\circ$ – $143^\circ$  MY 29) is associated with abnormally warm temperatures in both hemispheres, as well as enhanced traveling waves at upper levels. The sequence lasts for 14 sols, with a peak size of  $\sim 14,000,000 \text{ km}^2$  and a peak growth rate of  $\sim 1,800,000 \text{ km}^2/\text{sol}$ . This sequence may have triggered a unique Chryse sequence near its northern boundary.

Besides being the most important storm track outside the dust storm season, the ASV region (especially Solis) is an important secondary

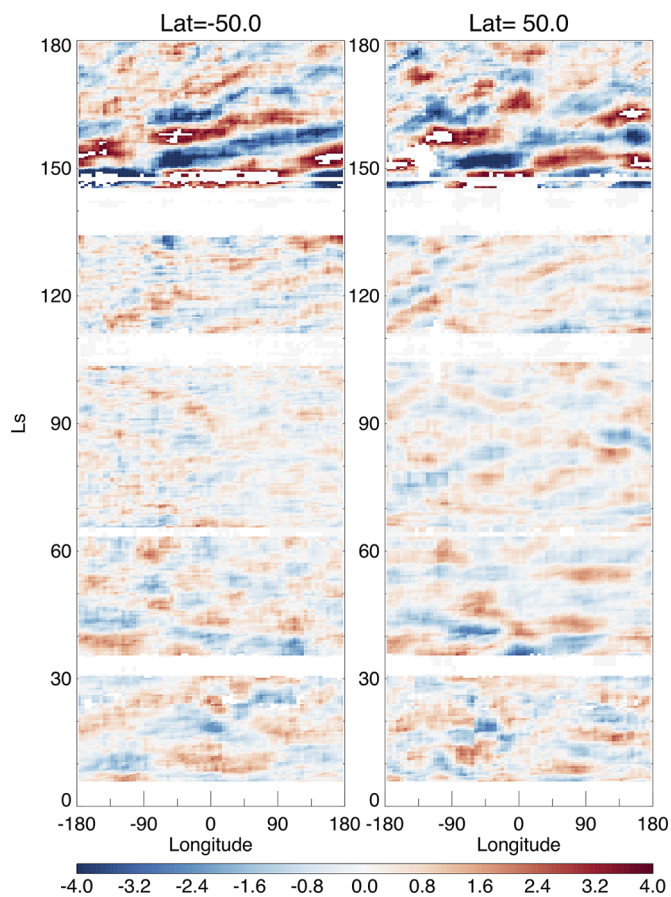


Fig. 14. MCS temperature anomalies associated with 15–30 day transient eddies at  $z \sim 45 \text{ km}$  for (left)  $50^\circ\text{N}$  and (right)  $50^\circ\text{S}$  as a function of longitude and  $L_s$  for MY 29.

lifting center for global dust storms (GDSs) during the dust storm season. This applies to the GDSs of MY 25 (Strausberg et al., 2005; Cantor, 2007), MY 28 (Wang and Richardson, 2015), as well as the latest in MY 34 (NASA/JPL-Caltech/MSSS, 2018). Although Solis contributed to all 3 GDSs since 1999, the ASV region becomes active only after the initial GDS lifting centers significantly perturb the atmosphere. In non-GDS years, the ASV region is inactive during northern fall and winter. Perhaps, during the dust storm season, lifting in Solis requires circulation enhancement by other dust lifting centers (Wang and Richardson, 2015). But, outside the dust storm season, the ASV sequences operate on their own.

The correspondence of the ASV storm track with the quasi-periodicity of the annular mode in the zonal-mean eddy kinetic energy may provide insight into inter-annual and inter-seasonal variability of dust activity. The difference in the periodicity of the terrestrial BAM (20–30 day cycle) and the 15–20 sol cycle of Mars could be related to the difference in radiative and dynamical timescales that would alter the speed of the baroclinic feedback mechanism that regulates the periodicity. The similarities and differences between our results and the terrestrial BAM warrant further investigation.

### Acknowledgments

MACDA v1 is available at <http://macdap.physics.ox.ac.uk>. The gridded optical depth data of Montabone et al. (2015) are available at [http://www-mars.lmd.jussieu.fr/mars/dust\\_climatology/index.html](http://www-mars.lmd.jussieu.fr/mars/dust_climatology/index.html). Version 1 MGS MOC MDGM is available at <https://dataverse.harvard.edu/dataset.xhtml?persistentId=doi:10.7910/DVN/WWRT1V>. Version 1 MRO MARCI MDGM is available at <https://dataverse.harvard.edu/dataset.xhtml?persistentId=doi:10.7910/DVN/G2VENZ>. Version 2 MRO MARCI MDGM is available at <https://astrogeology.usgs.gov/search/map/Mars/MarsReconnaissanceOrbiter/MARCI/MARS-MRO-MARCI-Mars-Daily-Global-Maps>. The version 2 MRO MARCI MDGM is supported by NASA's Planetary Data Archiving, Restoration, and Tools (PDART) program grant NNX16AG47G. The analysis in this study is supported by NASA's Mars Data Analysis Program (MDAP) grant 80NSSC17K0475. We thank two anonymous reviewers for helpful comments.

### Supplementary material

Supplementary material associated with this article can be found, in the online version, at doi:10.1016/j.icarus.2018.10.026.

### References

Banfield, D., Conrath, B., Gierasch, P., Wilson, R., Smith, M., 2004. Traveling waves in the martian atmosphere from MGS TES Nadir data. *Icarus* 170 (2), 365–403. <https://doi.org/10.1016/j.icarus.2004.03.015>.

Barnes, J.R., 1981. Midlatitude disturbances in the martian atmosphere: a second Mars year. *J. Atmos. Sci.* 38 (2), 225–234.

Battalio, M., Szunyogh, I., Lemmon, M., 2016. Energetics of the martian atmosphere using the Mars Analysis Correction Data Assimilation (MACDA) dataset. *Icarus* 276, 1–20. <https://doi.org/10.1016/j.icarus.2016.04.028>.

Battalio, M., Szunyogh, I., Lemmon, M., 2018. Wave energetics of the southern hemisphere of Mars. *Icarus* 309, 220–240. <https://doi.org/10.1016/j.icarus.2018.03.015>.

Cantor, B.A., 2007. MOC observations of the 2001 Mars planet-encircling dust storm. *Icarus* 186 (1), 60–96. <https://doi.org/10.1016/j.icarus.2006.08.019>.

Greybush, S.J., Gillespie, H.E., Wilson, R.J., 2019. Transient eddies in the TES/MCS Ensemble Mars Atmosphere Reanalysis System (EMARS). *Icarus* 317 (May 2018), 158–181. <https://doi.org/10.1016/j.icarus.2018.07.001>.

Guzewich, S.D., Toigo, A.D., Kulowski, L., Wang, H., 2015. Mars Orbiter Camera climatology of textured dust storms. *Icarus* 258, 1–13. <https://doi.org/10.1016/j.icarus.2015.06.023>.

Guzewich, S.D., Toigo, A.D., Wang, H., 2017. An investigation of dust storms observed with the Mars Color Imager. *Icarus* 289, 199–213. <https://doi.org/10.1016/j.icarus.2017.02.020>.

Hinson, D.P., Wilson, R.J., 2002. Transient eddies in the southern hemisphere of Mars. *Geophys. Res. Lett.* 29 (7), 3–6. <https://doi.org/10.1029/2001GL014103>.

Kass, D.M., Kleinböhl, A., McCleese, D.J., Schofield, J.T., Smith, M.D., 2016. Interannual similarity in the martian atmosphere during the dust storm season. *Geophys. Res. Lett.* 43 (May). <https://doi.org/10.1002/2016GL068978>.

Kleinböhl, A., Schofield, J.T., Kass, D.M., Abdou, W.A., Backus, C.R., Sen, B., Shirley, J.H., Lawson, W.G., Richardson, M.I., Taylor, F.W., Teanby, N.A., McCleese, D.J., 2009. Mars Climate Sounder limb profile retrieval of atmospheric temperature, pressure, and dust and water ice opacity. *J. Geophys. Res.* E 114 (10), 1–30. <https://doi.org/10.1029/2009JE003358>.

Kulowski, L., Wang, H., Toigo, A.D., 2017. The seasonal and spatial distribution of textured dust storms observed by Mars Global Surveyor Mars Orbiter Camera. *Adv. Space Res.* 59 (2), 715–721. <https://doi.org/10.1016/j.asr.2016.10.028>.

Lee, C., Richardson, M.I., Newman, C.E., Michael, A., 2018. The sensitivity of solsticial pauses to atmospheric ice and dust in the MarsWRF General Circulation Model. *Icarus* 311, 23–34. <https://doi.org/10.1016/j.icarus.2018.03.019>.

Lewis, S.R., Mulholland, D.P., Read, P.L., Montabone, L., Wilson, R.J., Smith, M.D., 2016. The solsticial pause on Mars: 1. A planetary wave reanalysis. *Icarus* 264, 456–464. <https://doi.org/10.1016/j.icarus.2015.08.039>.

Li, Y., Thompson, D.W., 2016. Observed signatures of the barotropic and baroclinic annular modes in cloud vertical structure and cloud radiative effects. *J. Clim.* 29 (13), 4723–4740. <https://doi.org/10.1175/JCLI-D-15-0692.1>.

Martin, L.J., Zurek, R.W., 1993. An analysis of the history of dust activity on Mars. *J. Geophys. Res.* 98 (E2), 3221–3246. <https://doi.org/10.1029/92JE02937>.

Montabone, L., Forget, F., Millour, E., Wilson, R.J., Lewis, S.R., Cantor, B.A., Kass, D.M., Kleinböhl, A., Lemmon, M.T., Smith, M.D., Wolff, M.J., 2015. Eight-year climatology of dust optical depth on Mars. *Icarus* 251, 65–95. <https://doi.org/10.1016/j.icarus.2014.12.034>.

Montabone, L., Marsh, K., Lewis, S.R., Read, P.L., Smith, M.D., Holmes, J., Spiga, A., Lowe, D., Pamment, A., 2014. The Mars analysis correction data assimilation (MACDA) dataset V1.0. *Geosci. Data J.* 1, 129–139. <https://doi.org/10.1002/gdj3.13>.

Mulholland, D.P., Lewis, S.R., Read, P.L., Madeleine, J.-B., Forget, F., 2016. The solsticial pause on Mars: 2 modelling and investigation of causes. *Icarus* 264, 465–477. <https://doi.org/10.1016/j.icarus.2015.08.038>.

Mulholland, D.P., Spiga, A., Listowski, C., Read, P.L., 2015. An assessment of the impact of local processes on dust lifting in martian climate models. *Icarus* 252, 212–227. <https://doi.org/10.1016/j.icarus.2015.01.017>.

NASA/JPL-Caltech/MSSS, 2018. 2018 Giant Dust Storm on Mars. <https://photojournal.jpl.nasa.gov/archive/PIA22519.gif>.

Pankine, A.A., 2015. The nature of the systematic radiometric error in the MGS TES spectra. *Planet. Space Sci.* 109–110, 64–75. <https://doi.org/10.1016/j.pss.2015.01.022>.

Pankine, A.A., 2016. Radiometric error and re-calibration of the MGS TES spectra. *Planet. Space Sci.* 134, 112–121. <https://doi.org/10.1016/j.pss.2016.10.015>.

Strausberg, M.J., Wang, H., Richardson, M.I., Ewald, S.P., Toigo, A.D., 2005. Observations of the initiation and evolution of the 2001 Mars global dust storm. *J. Geophys. Res.* 110 (E2), E02006. <https://doi.org/10.1029/2004JE002361>.

Thompson, D.W.J., Barnes, E.A., 2014. Periodic variability in the large-scale southern hemisphere atmospheric circulation. *Science* 343 (February), 641–645.

Thompson, D.W.J., Woodworth, J.D., 2014. Barotropic and baroclinic annular variability in the southern hemisphere. *J. Atmos. Sci.* 71 (4), 1480–1493. <https://doi.org/10.1175/JAS-D-13-0185.1>.

Toigo, A.D., Richardson, M.I., Wang, H., Guzewich, S.D., Newman, C.E., 2018. The cascade from local to global dust storms on Mars: temporal and spatial thresholds on thermal and dynamical feedback. *Icarus* 302, 514–536. <https://doi.org/10.1016/j.icarus.2017.11.032>.

Wang, H., Ingersoll, A.P., 2002. Martian clouds observed by Mars Global Surveyor Mars Orbiter Camera. *J. Geophys. Res.* 107 (E10), 5078. <https://doi.org/10.1029/2001JE001815>.

Wang, H., Richardson, M.I., 2015. The origin, evolution, and trajectory of large dust storms on Mars during Mars years 24–30 (1999–2011). *Icarus* 251, 112–127. <https://doi.org/10.1016/j.icarus.2013.10.033>.